GEOPHYSICAL RESEARCH LETTERS, VOL. 39, DOI:10.1029/2012GL051312, 2012

Auxiliary material for "Earth-based detection of Uranus' aurorae"

L. Lamy[1], R. Prangé[1], K. C. Hansen[2], J. T. Clarke[3], P. Zarka[1], B. Cecconi[1], J. Aboudarham[1], N. André[4], G. Branduardi-Raymont[5], R. Gladstone[6], M. Barthélémy[7], N. Achilleos[8], P. Guio[8], M. K. Dougherty[9], H. Melin[10], S. W. H. Cowley[10], T. S. Stallard[10], J. D. Nichols[10], G. Ballester[11]

S1. Terrestrial and Jovian auroral responses

The characteristics of the CMEs shown in Figure 2a (direction, angular width, median speed) were obtained from the STEREO/SECCHI A and B CME lists of the CACTus catalogue[1] [*Robbrecht et al.*, 2009]. Events A and C were associated with X-class solar flares (not shown). Earth-based observations of SOHO/LASCO, also listed in the same catalogue, indicate a halo (angular width of 360°) for events A and C, and a partial halo (angular width of ∼ 240°) for event B.

S1.1. The Earth

The auroral power precipitated in both terrestrial hemispheres, displayed in Figure 2b (left), was extrapolated from polar measurements of NOAA/POES satellites, ranging from 5 to 230 GW per hemisphere, yielding auroral radiated powers approximately 10 times less. Southern and northern powers are strongly conjugate (0.81 Spearman's rank correlation coefficient), and their sum displays a good correlation with the ram pressure of the solar wind (0.59), which increases (0.64) when only considering anti-parallel configurations between magnetospheric and interplanetary magnetic fields at the subsolar magnetopause (the green portions in Figure 2b, right) [*Boudouridis et al.*, 2005, and refs therein]. Hemispheric powers increased by a factor of 30 to 60 during events A, B and C. This high variability results from the strong control exerted by the solar wind on the terrestrial magnetosphere, owing to the nature of the substorm activity driving aurorae which is triggered by reconnection processes in the magnetotail.

[1]LESIA, Obs. de Paris, CNRS, UPMC, Université Paris Diderot, Meudon, France

[2]Department of Atmospheric, Oceanic and Space Sciences, University of Michigan, Ann Arbor, Michigan, USA.

[3]Center for Space Physics, Boston University, Boston, Massachusetts, USA.

[4]Institut de Recherche en Astrophysique, CNRS, Université Paul Sabatier, Toulouse, France

[5]University College London, Mullard Space Science Laboratory, Dorking, UK

[6]Southwest Research Institute, San Antonio, USA

[7]Institut de Planétologie et d'Astrophysique de Grenoble, CNRS, Université Joseph Fourier, Grenoble, France

[8]University College London, London, UK

[9]Blackett Laboratory, Imperial College London, London, UK

[10]Department of Physics and Astronomy, University of Leicester, Leicester, UK

[11]Lunar and Planetary Laboratory, University of Arizona, USA

0094-8276/12/2012GL051312$5.00

S1.2. Jupiter

The Waves experiment onboard the STEREO spacecraft continuously monitors heliospheric radio emissions up to 16 MHz [*Bougeret et al.*, 2008], including Jovian decametric (DAM), hectometric (HOM) and kilometric (KOM) quasi-permanent auroral emissions [*Zarka et al.*, 2004]. From 6 September (solar emission of event A) to 8 October (predicted arrival of event C at Jupiter), the Earth-Sun-Jupiter angle varied from 58° to 19°, roughly matching the typical angular extent of CMEs [*Robbrecht et al.*, 2009]. Despite being distant from Jupiter by ∼5 AU, both STEREO A and B detected Jovian radio auroral signatures for each of pressure fronts A, B and C, providing useful indications for predictions at further distances. Periods of time when Jovian emissions were observed above the background level are indicated by orange-shaded intervals in Figure 2c, (right). They generally occurred within ±12 h of the predicted times, while fainter emissions were observed for longer intervals. In the example displayed in Figure 2c (left), measurable Jovian signals are visible between DOY (day of year) 268.75 and 269.3. Precisely, a pattern of non-Io (auroral) arc-like structures truncated at 16 MHz appears around 19:00 UT of DOY 268, and repeats one planetary rotation later. Interestingly, while non-Io DAM, HOM and KOM emissions have been considered as distinct emissions in the past [*Zarka*, 1998, and refs therein], the Jovian spectrum here brightened continuously from 16 MHz to 600 kHz, from DAM to KOM, suggesting a common origin.

The Nançay decameter array[2] performs a long-term monitoring of Jovian radio emissions over 10-40 MHz, when the planet is visible (∼8 h per day). Taking advantage of combined STEREO/Nançay observations of an Io-D arc (southern hemisphere radio emission triggered by the Io-Jupiter interaction) observed on 3 October, we calibrated the signal measured by STEREO with the absolute flux measured by Nançay. In the example displayed in Figure 2c (left), this yielded a flux of $\sim 10^{-19}$ W.m^{-2}.Hz^{-1} (normalized at 1 AU) at 3-4 MHz, reaching the 1% occurrence level of emission [*Zarka et al.*, 2004], at twice the background level. Comparable results were obtained for events B and C. Jovian emissions therefore intensified by at least a factor of 2, in agreement with previous estimates [*Gurnett et al.*, 2002; *Clarke et al.*, 2009]. This lower variability with respect to the Earth illustrates the more modest influence of the solar wind on Jupiter's magnetosphere, which is instead dominated by internal processes.

Finally, combined Chandra observations of Jovian X-ray aurorae were also scheduled in advance and obtained around the arrival of shock B. Their analysis will provide complementary insights on the Jovian auroral response to the solar wind (G. Branduardi-Raymont et al., manuscript in preparation, 2012).

S2. HST data

HST FUV observations of Uranus obtained in November 2011 consisted of 17 orbits, composed of 9 STIS identical visits and 8 ACS ones.

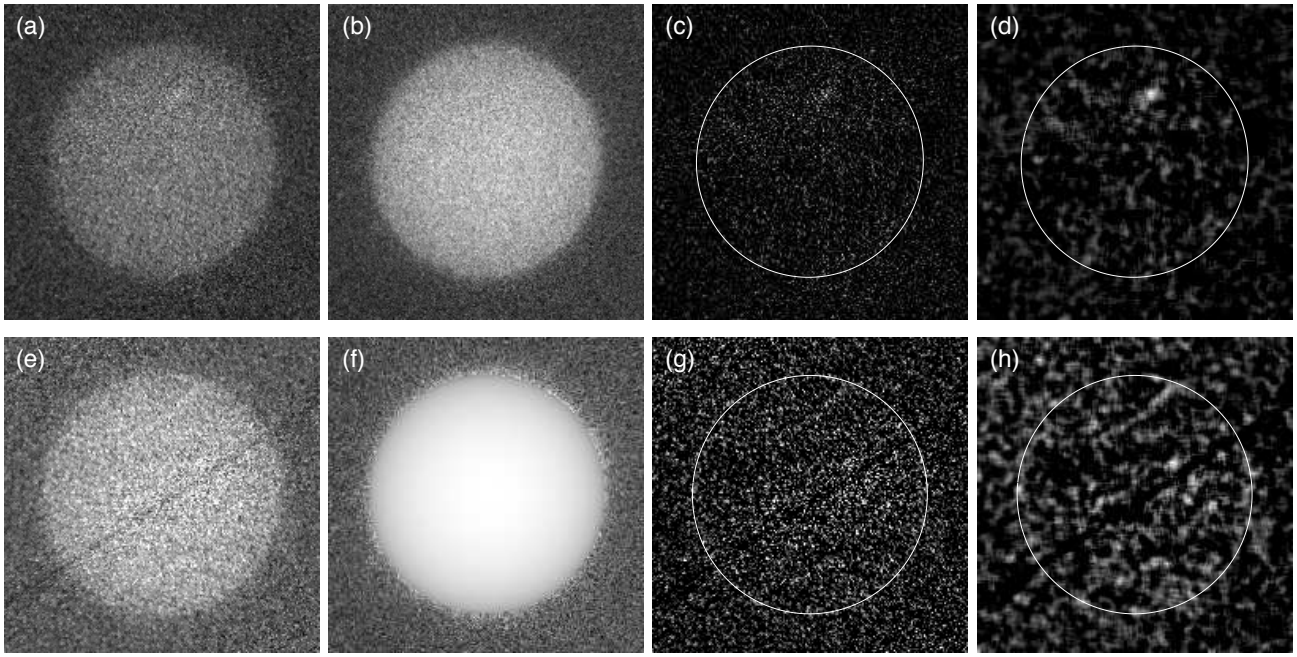

Figure S1. Processing of HST/STIS calibrated images obtained on (a,b,c,d) 29 November 2011 and (e,f,g,h) 29 July 1998, respectively. Panels (a,e) show raw images in counts (arbitrary gray scale), identical to Figures 3b and 3c (top). Panels (b,f) display models of reflected background, each fitted to the disc emission of corresponding raw images. Panels (c,g) show the difference between raw images and background models, and the planetary limb is plotted in white. Panels (d,h) reproduce panels (c,g) with an additional smoothing over 5 pixels. They are identical to Figures 3b and 3c (bottom).

STIS visits each include (i) one FUV spectrum spanning the range 115 to 173.6 nm, acquired with the G140L grating and the 2 arcsec large slit over 1100 s, and (ii) one image acquired with the clear filter (137 nm central wavelength, 32 nm FWHM, including H Ly-α) over 1000 s. Both images and spectra were acquired in the time-tag mode, which provides the timing of photons recorded on the Multi-Anode Multichannel Array (MAMA) detector at a time resolution of 125 microseconds.

ACS visits each include a series of 6 images using 3 different longpass filters : (j) two images acquired with the F140LP filter (152.7 nm central wavelength, 29.4 nm FWHM, rejecting H Ly-α) each integrated over 450 s, (jj) three images acquired with the blank F115LP filter (140.6 nm central wavelength, 35.5 nm FWHM, including H Ly-α) each integrated over 400 s and (jjj) one image acquired with the F165LP filter (175.8 nm central wavelength, 20.3 nm FWHM, rejecting most of H_2 emission) integrated over 360 s. These filters were aimed at observing H Ly-α and H_2 emissions together (F115LP), H_2 alone (F140LP), H Ly-α alone (obtained through the difference between F115LP and F140LP), and the disc background (F165LP).

This study uses data calibrated through the STSci pipeline, and focuses on the analysis of images. A model of reflected background was built for the three raw images displayed in Figure 3, as illustrated in Figure S1 for two of them. Figures S1a and S1e are identical to Figures 3b and 3c (top), respectively. For observations obtained in 2011, we built an empirical model (Figure S1b). This was not possible to achieve for the more limited set of HST observations obtained in 1998, for which we built a numerical model instead, fitted to the disc emission with Minnaert functions [*Vincent et al.*, 2000] and convolved by the STIS point spread function. This model was completed with a scaled empirical model beyond the planetary limb (Figure S1f). Figures S1c and S1g show the difference between raw images and background models. Figures S1d and S1g, identical to Figures 3b and 3c (bottom), have been additionally smoothed over 5 pixels to improve the contrast.

S3. Analysis of auroral signatures

S3.1. Identification of auroral features

Because of the distance of Uranus to the Earth, its low level of emission and short exposures (17 to 18 min), the planetary signal measured by HST is faint and noisy, which in turn renders any unambiguous identification of auroral features difficult, contrary to similar observations of Jupiter and Saturn.

For the localized bright spots observed in STIS images (Figures 3a,b) corrected for background, the level of emission per pixel reaches up to 3 to 5 σ above the noise level, yielding clear positive detections. In contrast, for the fainter elongated features observed in Figure 3c, the signal per pixel essentially lies between 1 σ and 3 σ. To overcome this ambiguity, we integrated the signal along model ovals to increase the signal-to-noise ratio, in order to unambiguously validate candidates for auroral features. Figure S2 shows the results of tests on the northern and southern auroral structures of Figure 3c. Model ovals were obtained from empirical fits of the observed features with two partial ellipses, excluding emission along the limb to avoid any possible bias originating from background subtraction. Then the mean signal integrated along the so-determined oval was compared to the mean signal computed along 1000 identical ovals, randomly shifted (within a distance of 75 pixels from the planet's center) and rotated (from 0° to 360°) within the planetary disc, with the condition that at least 90% of their surface lies on the disc. Random distributions were obtained with the randomn IDL routine, based on the Box-Muller method for generating normally-distributed (gaussian) random numbers. Results displayed in Figures S2c,d and S2e,f

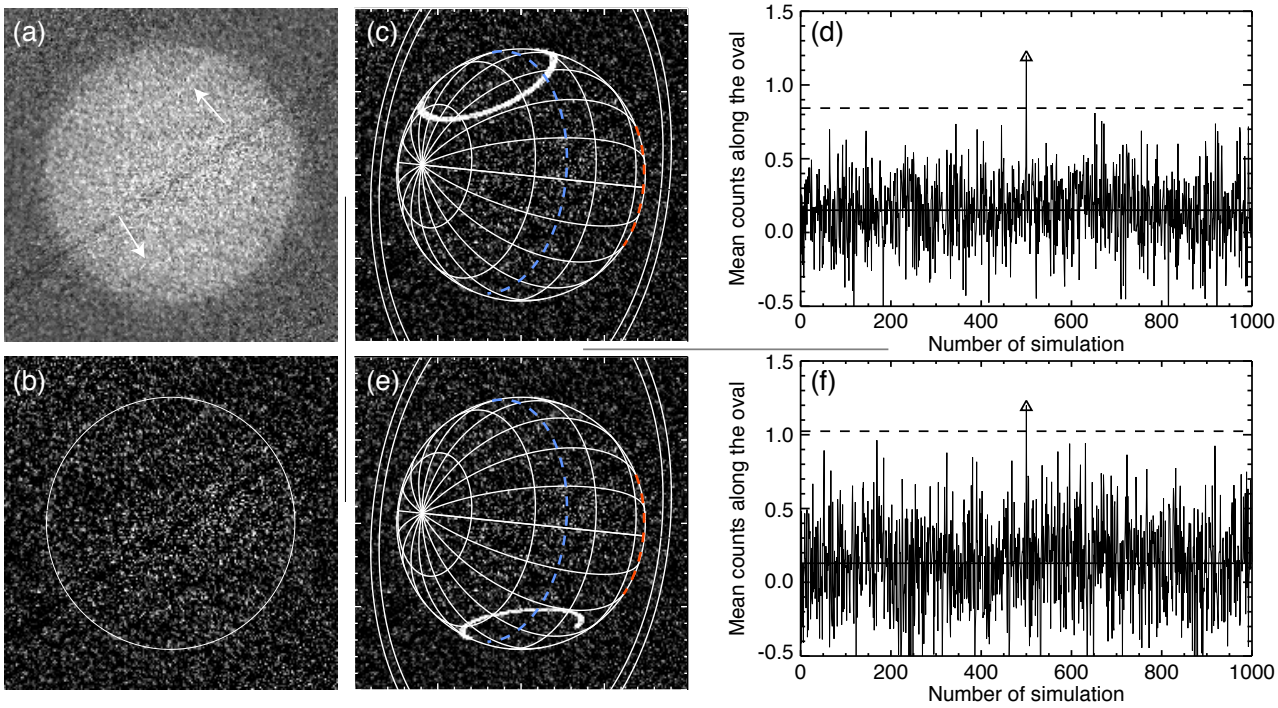

Figure S2. (a,b) HST/STIS images identical to Figures S1e and S1f. (c) Same image as panel (b) together with a model northern oval superimposed in white, and a grid of planetocentric coordinates at the 1-bar level. Red and blue dashed lines mark the latitudes of the northern and southern magnetic poles respectively. (d) Average counts along the model oval displayed in panel (c) for 1000 separate simulations (x-axis). For each run, the model oval has been shifted and rotated randomly, with the condition that at least 90% of the oval lies on the planetary disc, before integration. The position corresponding to the reference oval is indicated by a diamond. Black and dashed horizontal lines show the average and the 3σ level, respectively. The diamond lies at $\sim 5\sigma$. (e,f) Same as (c,d) for a model southern oval. The integrated signal-to-noise ratio lies around 4σ.

yield positive detection of both ovals, with integrated signal-to-noise ratios reaching ~ 4 to $\sim 5\sigma$. These values shall be taken as lower limits, as the investigated auroral features may not be continuous and/or elliptically shaped.

The planetocentric coordinates of all auroral signatures discussed in the main text are taken to the 1-bar level. We checked that these coordinates derived at 1000 km above the 1-bar level instead (a standard order of magnitude for giant planets), brings less than a 5° uncertainty. Fitted features in Figures S2c and S2e are considered as distinct, as their size is smaller than their separation in longitude. They are hereafter identified as N and S ovals, as their center lie in N and S hemispheres respectively, with a larger N oval.

S3.2. Constraints on the rotation period

Assuming that the auroral ovals are centered on the magnetic poles, the position of their center brings a new constraint to the Uranian rotation period and the ULS longitude system. We consider the N oval of Fig. 3c. The uncertainty on the original rotation period 17.24 ± 0.01 h, applied to the interval ranging from the 24 January 1986 18:00 UT (flyby of Voyager 2) [*Ness et al.*, 1986] to the 29 July 1998 06:16:03 UT (mean time of Fig. 3c), exceeds 8 planetary rotations. We can thus estimate 8 rotation periods by extending the ULS system to make the N magnetic pole match the longitude of the N oval's center. Assuming that this longitude is known at ±45° then yields an uncertainty on the derived rotation periods improved to $\pm 4 \times 10^{-4}$ h. These preliminary results summarize as $P_i = 17.2302 + i \times 0.0027 \pm 0.0004$ h (i = 0 to 7).

Nonetheless, our original assumption that the center of the N oval provides a reliable estimate of the N magnetic pole can be questioned by the observed discrepancy of 25° in latitude. Additionally, if the planetary magnetic field were subject to any secular change, the motion of the N magnetic pole would even change the meaningness of the rotation period. More robust conclusions therefore require the identification of more auroral ovals at different epochs.

Notes

1. http://secchi.nrl.navy.mil/cactus/
2. http://www.obs-nancay.fr

References

Boudouridis, A., E. Zesta, L. R. Lyons, P. C. Anderson, and D. Lummerzheim, Enhanced solar wind geoeffectiveness after a sudden increase in dynamic pressure during southward IMF orientation, *Journal of Geophysical Research (Space Physics)*, *110*(A9), A05214, doi:10.1029/2004JA010704, 2005.

Bougeret, J. L., et al., S/WAVES: The Radio and Plasma Wave Investigation on the STEREO Mission, *Sp. Sci. Rev.*, *136*, 487–528, doi:10.1007/s11214-007-9298-8, 2008.

Clarke, J. T., et al., Response of Jupiter's and Saturn's auroral activity to the solar wind, *J. Geophys. Res.*, *114*(A13), A05,210, doi:10.1029/2008JA013694, 2009.

Gurnett, D. A., et al., Control of Jupiter's radio emission and aurorae by the solar wind, *Nature*, *415*, 985–987, 2002.

Ness, N. F., M. H. Acuna, K. W. Behannon, L. F. Burlaga, J. E. P. Connerney, and R. P. Lepping, Magnetic fields at Uranus, *Science*, *233*, 85–89, doi:10.1126/science.233.4759.85, 1986.

Robbrecht, E., D. Berghmans, and R. A. M. Van der Linden, Automated LASCO CME Catalog for Solar Cycle 23: Are CMEs Scale Invariant?, *Astrophys. J.,* , *691*, 1222–1234, doi: 10.1088/0004-637X/691/2/1222, 2009.

Vincent, M. B., et al., Mapping Jupiter's Latitudinal Bands and Great Red Spot Using HST/WFPC2 Far-Ultraviolet Imaging, *Icarus*, *143*, 189–204, doi:10.1006/icar.1999.6232, 2000.

Zarka, P., Auroral radio emissions at the outer planets: Observations and theories, *J. Geophys. Res.,* , *103*, 20,159–20,194, doi:10.1029/98JE01323, 1998.

Zarka, P., B. Cecconi, and W. S. Kurth, Jupiter's low-frequency radio spectrum from Cassini/Radio and Plasma Wave Science (RPWS) absolute flux density measurements, *Journal of Geophysical Research (Space Physics)*, *109*(A18), A09S15, doi: 10.1029/2003JA010260, 2004.